Corrosion Resistance, Composition, and Stratification of Passive Films: Ni-22Cr and Ni-22Cr-6Mo Alloys Passivated and Exposure Aged in Acidic Chloride Solutions

Journal of The Electrochemical Society, 2024 **171** 011505

Corrosion Resistance, Composition, and Stratification of Passive Films: Ni-22Cr and Ni-22Cr-6Mo Alloys Passivated and Exposure Aged in Acidic Chloride Solutions

Keithen Orson,[1] Elena Romanovskaia,[1,2] Anna Costine,[1] Junsoo Han,[3] Kevin Ogle,[4] John R. Scully,[1,2] and Petra Reinke[1,z]

[1]*Department of Materials Science and Engineering, University of Virginia, 22903 Charlottesville, Virginia, United States of America*
[2]*Center for Electrochemical Science and Engineering, University of Virginia, 22903 Charlottesville, Virginia, United States of America*
[3]*Sorbonne Université, Laboratoire Interfaces et Systèmes Electrochimiques, F-75005 Paris, France*
[4]*Chimie ParisTech, PSL University, Institut de Recherche Chimie Paris (IRCP), F-75005 Paris, France*

Ni-Cr based super-alloys have exceptional corrosion resistance, which is further improved with Mo alloying. The correlation between passive layer performance and composition was studied to gain a deeper mechanistic understanding of the role of Mo by comparing the behavior of Ni-22Cr to Ni-22Cr-6Mo (wt%) alloys. The passive layers were formed using galvanostatic holds to create fast and slow growth conditions using high and low current densities. A potentiostatic hold was added to initiate exposure aging. The passive film was characterized using electrochemical impedance spectroscopy (EIS), linear sweep voltammetry (LSV), atomic emission spectro-electrochemistry (AESEC), and X-ray photoelectron spectroscopy (XPS). Combined electrochemical and XPS characterization offered insight in cation concentrations and stratification, bonding states (oxide, hydroxide), and their modulation as a function of electrochemical conditions and performance. Most importantly: (i) Mo addition enhanced Cr(III) bound in oxide, (ii) fast growth conditions resulted in less corrosion resistant films, and (iii) exposure aging increased Cr-enrichment and reduced stratification of Mo-cations. The correlation between passive film performance and Cr, Ni, and Mo oxidation states, bonding, oxide-hydroxide contributions, and stratification is discussed. Generally accepted correlations, such as Cr-cation concentration and performance of the passive layer, have to be reexamined in order to account for the complex chemical make-up of the passive layer.

 [DOI: 10.1149/1945-7111/ad1d28]

Manuscript submitted November 12, 2023; revised manuscript received January 7, 2024. Published January 25, 2024.

Supplementary material for this article is available online

Corrosion resistance is a key design criterion for steels, Ni-based superalloys, and Ni-Al alloys. Ni-Cr alloys, a type of Ni-based superalloy, are useful for their mechanical and thermal properties, but they are exceptional because of their corrosion resistance. Ni-Cr based alloys are selected for applications such as gas turbines and fuel cells, where alloys are subjected to corrosive environments and elevated temperatures.[1] The resistance of Ni-Cr alloys to aqueous chloride exposure is especially important for marine applications.

Understanding how the passive layer develops under aqueous exposure conditions is crucially important for improving corrosion resistance and ultimately achieve rational design of corrosion-resistant alloys.[2,3] The Ni-Cr alloy system is protected by the formation of a passive layer with oxide and hydroxide contributions. Chromium in the alloy contributes to the formation of a particularly resistant protective passive film, owing to the formation of Cr_2O_3.[4] The addition of minor alloying elements (MAE) can play an outsized role in corrosion protection.[5–7] In the Ni-Cr system, Mo and W are especially beneficial by preventing breakdown events and pitting[5] which is critical for performance in chloride solutions.[8,9] Mo is not the primary passivating element but is incorporated in the passive films as molybdenum oxides and hydroxides, modulating many of its characteristics.[10,11]

The role of Mo is multifaceted and can impact various aspects of passive film formation and function. Mo and W have been reported to mitigate pitting by re-passivation and repair of pitting sites[5,8] to stabilize the passive layer by serving as aliovalent cations which can sequester defects, to modify reactant transport such as oxygen in the passive layer,[12] limit the dissolution of Cr into the aqueous phase which favors the formation of chromia,[13] and are relevant for overall stabilization of the passive layer.[5,14] The effects of both elements on corrosion resistance in the Ni-Cr system appear to be quite similar but can differ in magnitude.[5,8,12] Understanding of complex phenomena in passivation takes a step towards being able to design novel, corrosion resistant alloys using major as well as minor alloying additions.[2]

The primary passive layer components for the Ni-superalloy system are $Ni(OH)_x$, Cr_2O_3, and $Cr(OH)_x$[15] and $Ni_{1-x}Cr_xOy$ with mixed cation populations or spinel in some instances. In most Ni-based superalloys NiO is not present in the passive layer,[15] and the Cr-components dominate.[8,16] A layering scheme with hydroxides on top is a common model discussed in literature,[10,17–19] and a passive layer rich in $Cr(OH)_3$ can over time contribute to the nucleation of Cr-oxides.[6,20,21] The addition of Mo (or W) generally increases the fraction of Cr(III)[8,22,23] in the passive film.[24] Li et al.[3] report a modulation of Cr and Mo dissolution rates, which can overall improve passivity and strongly depends on the specific conditions of the electrochemical process and associated dissolution equilibria.

Recent long-term studies with exposure times up to 10^6 s for the passive film growth and concomittant transformation in the Ni-Cr alloy systems[7,25,26] showed that Ni(II) formed early, Cr(III) enrichment occurred over long exposures, and the passive film composition underwent significant changes with exposure time. Cr oxides and hydroxides were formed at short passivation times, and the spinel $NiCr_2O_4$ was generally detected at much longer times and at certain applied potentials in the passive range.[7,25,26] The nanostructure of the passive film formed on Ni-Cr and Ni-Cr-Mo alloys has been studied with Transmission Electron Microscopy (TEM) and this work showed the dissolution of oxygen in the metal lattice below the oxide.[13] Mo addition also affects the diffusivity of oxygen through the passive film and promotes corundum formation which can be associated with chromia, but also Ni-rich solute captured phases.[13] The presence and distribution of Mo as an aliovalent cation within the passive layer is tightly connected to the various

[z]E-mail: pr6e@virginia.edu

mechanisms proposed for its beneficial action. The role of the various oxidation states, mostly Mo(IV) and Mo(VI), and their distribution throughout the passive layer are discussed in the literature for Ni-Cr-Mo[8,22,27,28] as well as for Fe-Cr-Mo systems.[29,30]

In the work presented here the passive layers are grown under different kinetic regimes, slow and fast, which offers insight across a wide range of environmental conditions. These conditions are analogous to rapid repair after exposing bare metal or long duration, slow exposure to NaCl with a mild oxidizer such as O_2. While some studies are reported in the literature regarding open circuit potential[10,11,31–33] and potentiostatic film growth,[3,34] the understanding of how high and low galvanostatic hold current density and, in turn, growth kinetics affect the passive film is limited.

Our work establishes the relation between growth kinetics, passive layer components and subsequent electrochemical assessment of protectiveness. The relevance of various kinetic regimes has previously been discussed in the framework of the solute capture mechanism[35] where the incorporation of different elements in the passive layer is influenced by a reaction akin to solidification from liquid where elements are quenched into an amorphous solid solution. This effect has been demonstrated for the Ni-Cr-Mo system,[13] and it is important to understand how a non-equilibrium growth process, or growth kinetic regime , affects the composition and protectiveness of the passive film.

Two high Cr-content alloys, Ni-22Cr and Ni-22Cr-6Mo (all compositions given in wt%), are exposed to four different corrosion conditions defined by the electrochemical parameters and designed to probe a wide range of passive layer growth conditions. The ternary alloy includes Mo to assess its impact on passivity under otherwise identical electrochemical conditions. The different kinetic regimes are accessed by modulation of the passive film growth during an initial galvanostatic growth step. For half of the samples this step is followed by a potentiostatic hold critically at a passive potential below transpassivity. This hold enables exposure aging of the passive film. These two alloys were therefore exposed to four different corrosion conditions covering a wide range of reaction regimes. The passive film properties are interrogated *ex situ* by Electrochemical Impedance Spectroscopy (EIS), Linear Sweep Voltammetry (LSV), and atomic emission spectroelectrochemistry (AESEC). The electrochemical findings are correlated with detailed surface composition and species analysis with X-ray Photoelectron Spectroscopy (XPS).

Experimental

The samples were polycrystalline, solid solution FCC Ni-alloys with the compositions Ni-22Cr and Ni-22Cr-6Mo wt.%. These alloys are denoted as Ni-22Cr and Ni-22Cr-6Mo, respectively. The compositions in at. % are Ni-24at%Cr and Ni-24.7at%Cr-3.7at%Mo. The alloys were arc-melted, cast, cold rolled, solutionized at 1300 °C for 1 h, recrystallized at 800 °C for 48 h, and sectioned. Prior to each experiment, the samples were ground to 1200 grit using SiC paper and then gradually polished with 3, 1 and 0.1 μm diamond suspension. The samples were then ultrasonically cleaned with isopropanol, rinsed with deionized water produced by a Milli-Q system having resistivity of 18.2 MΩ cm, and deaerated with nitrogen gas before being placed into a vertical flat cell window for electrochemical studies. The solution used in the electrochemical experiments was 0.1 M NaCl adjusted to pH 4 using 1 M HCl. All solutions were prepared with reagent grade chemicals dissolved in the Milli-Q system deionized water. The solutions were deaerated with bubbling N_2 gas for 30 min prior to each test, and N_2 bubbling was continued throughout the electrochemical experiments.

The electrochemical exposure conditions and analysis methods are summarized in Fig. 1, and passivation conditions and sample labels are given in Table I. We included (a) variable driving force under galvanostatic fixed rate conditions to access different kinetic growth regimes, (b) and subsequently with fixed potential driving force, decaying growth rate (potentiostatic) conditions which corresponds to "exposure aging." Electrochemical control was maintained with a Gamry Reference 600 potentiostat. The electrochemical cell for experiments was a three-electrode flat cell with a Pt mesh counter electrode and saturated calomel reference electrode (SCE). The E-log i passivation behavior of Ni-22Cr and Ni-22Cr-6Mo shown in Fig. 2a shows the potential dependent reactivity of each system. The imaginary part of the impedance Z″ (Fig. 2b) was recorded in a separate measurement at $f = 1$ Hz over the same potential range as the polarization experiment from -1.3 V_{SCE} to $+0.8$ V_{SCE} at 1 mV s^{-1}. The $-Z''$ value is linearly proportional to oxide thickness assuming a pseudo capacitor model to describe the passive film or interphase sandwiched between the metallic conductor and electrolyte as discussed below.

The galvanostatic growth experiment was conducted using the following experimental protocol. The initial cathodic reduction step was performed at -1.3 V_{SCE} for 600 s to minimize the presence of air-formed native oxide films on the surface.[20,24,36] Following this, a constant current of 0.1 μA cm^{-2} (slow growth) or 100 μA cm^{-2} (fast growth) was applied galvanostatically to grow the oxide within the passive region until the potential required to maintain the current density reached $+0.2$ V_{SCE}. The potentiostatic growth rate fixed the potential driving force by applying a voltage of $+0.2$ V_{SCE} within the passive region for time periods of 10 ks. Hence, the maximum potential driving force was the same in each process.

For each electrochemical condition, four sets of analysis and characterization steps each of the corrosion product and passive film were conducted and are summarized in the flow chart in Fig. 1: (a) full spectrum electrochemical impedance spectroscopy (EIS), (b) linear sweep voltammetry (LSV) after the passive film formation, (c) X-ray photoelectron spectroscopy (XPS) analysis, (d) atomic emission spectroelectrochemistry (AESEC) analysis. These experiments interrogated the protectiveness of passive layers grown under the driving force–oxidation rate conditions described above in acidic Cl^- solution. The EIS measurements were started immediately after the galvanostatic potential reached $+0.2$ V_{SCE} and were conducted in the frequency range from 100 kHz to 1 mHz with 5 points per decade using a 20 mV sinewave perturbation. LSV was performed after the galvanostatic growth and 30 min of additional open circuit potential (OCP) hold by sweeping upward in the potential range from -0.2 V_{SCE} to $+1.0$ V_{SCE} at a scan rate of 1 mV s^{-1}.

In a first set of samples, only a galvanostatic passive film growth was applied, with an applied current of either 0.1 or 100 μA cm^{-2}, which are referred to as "S" for slow and "F" for fast growth, respectively. The second set of samples was prepared by imposing an additional potentiostatic hold immediately after the galvanostatic growth. A full summary of conditions is given in Table I. The potentiostatic hold was carried out with the single frequency EIS (SF-EIS) method, and the applied potential was $+0.2$ V_{SCE} with a frequency of 1 Hz and an AC amplitude of 20 mV. Following SF-EIS, the EIS spectrum was acquired at the same potential, $+0.2$ V_{SCE}, from 100 kHz to 1 mHz. The imaginary impedance data (Z″) can then be correlated with an oxide thickness using an electrical equivalent circuit model developed for Ni-Cr alloys.[20] The choice of frequency and use of SF-EIS for oxide thickness calculations is discussed in detail in previous work.[6,24,37] Oxide thickness was estimated using the relation:

$$l_{ox}(t) = \frac{-Z''(t)(2\pi f \epsilon \varepsilon_o)^{\alpha} A}{\rho_{\delta}^{1-\alpha} \sin\left(\frac{\alpha\pi}{2}\right)[1 + 2.88(1-\alpha)^{2.375}]} \quad [1]$$

where f is the applied frequency, ε is the dielectric constant ,[38] ε_o is the vacuum permittivity, and α is the constant phase element (CPE) exponent. A represents the exposed sample area, ρ_δ is the boundary interfacial resistivity, and Z″(t) is the imaginary component of SF-EIS at a given time. The dielectric constant used for each passive film grown on Ni-22Cr and Ni-22Cr-6Mo was based on a weighted average of the values for the different oxides/hydroxides detected

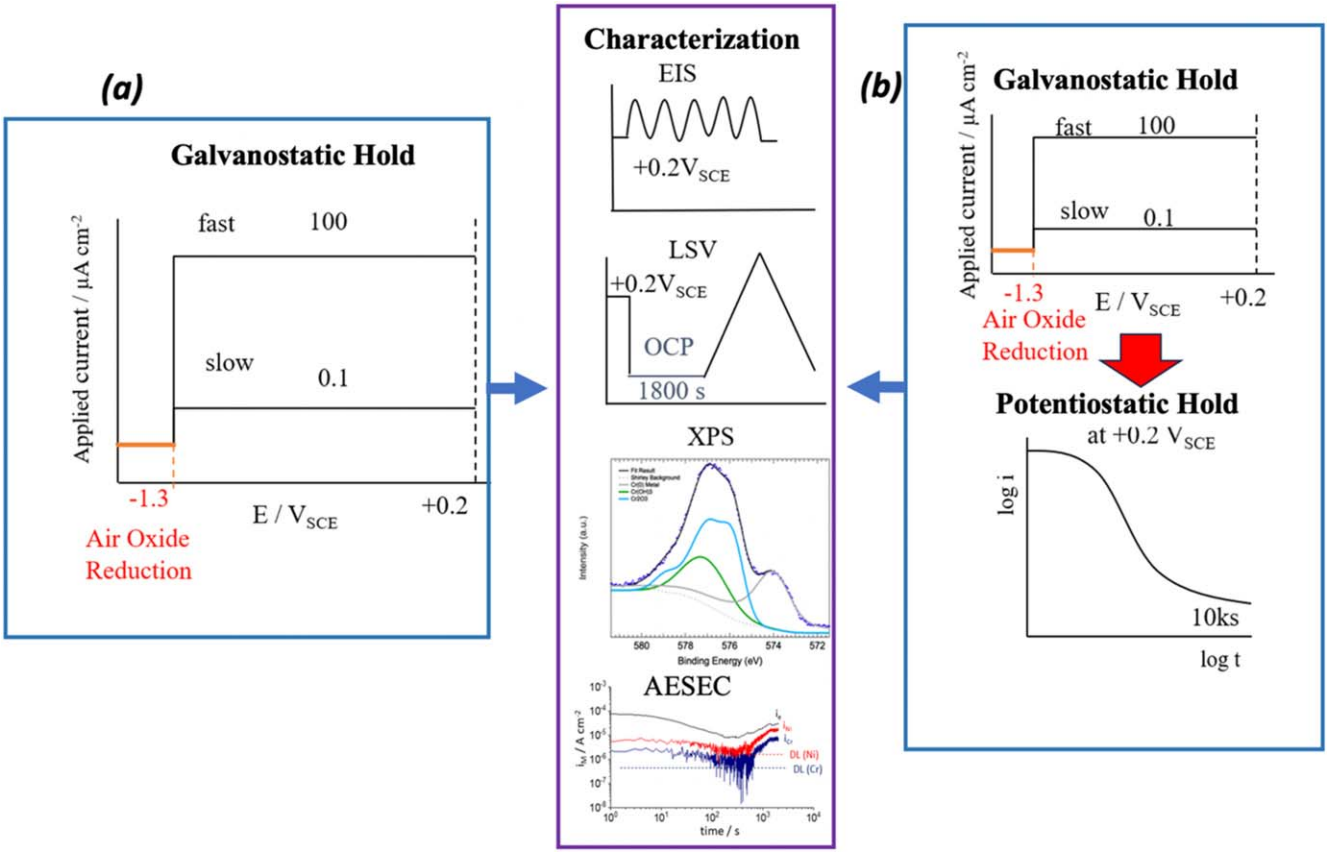

Figure 1. Experimental procedure: (a) galvanostatic growth; (b) galvanostatic growth followed by potentiostatic hold with subsequent set of experiments and characterization. Characterization panel in the center includes electrochemical impedance spectroscopy (EIS), linear sweep voltammetry (LSV), (c) X-ray photoelectron spectroscopy (XPS) analysis, (d) atomic emission spectro-electrochemistry (AESEC) analysis.

with XPS. The following values for dielectric constants were used: $\varepsilon(Cr_2O_3) = 30$,[34] $\varepsilon(NiO) = 11.9$[39] and $\varepsilon Ni(OH)_2 = 2.7$.[40,41] The details of oxide thickness determination have been previously discussed.[41]

Equation 1 gives the expression for the application of SF-EIS to the analysis of passive film growth. From measurements of Z'' at a frequency f over a specific amount of time, it is possible to measure l_{ox} variations for the exposed sample area. The CPE constant, α, is found by fitting an EIS spectrum acquired across a range of high to low frequencies to a circuit model. The frequency of 1 Hz was chosen to measure Z'' corresponding to the characteristic one for the passive film growth. These parameters are highly sensitive to the specifics of an electrochemical system and enable broad application of SF-EIS for measurements of passive film growth. ρ_δ has to be quantified for each alloy and solution environment combination but $l_{ox}(t)$ only weakly depends on this α is very close to 1 for a capacitive CPE. Less significantly, ρ_δ must also be quantified for each alloy and solution environment combination but $l_{ox}(t)$ is only marginally dependent on this parameter, as $l_{ox}(t) \propto {\rho_\delta}^{\alpha-1}$ and α is very close to 1 for a capacitive CPE.

AESEC was used to monitor the elemental dissolution rates during the galvanostatic and potentiostatic hold experiments. The principles of this technique are described elsewhere.[36,42,43] The specimen was placed in a custom designed electrochemical flow cell. The electrolyte containing the dissolved species from the specimens was transferred to an inductively coupled plasma atomic emission spectrometer (ICP-AES, Ultima 2C^{TM}, Horiba Jobin Yvon). Elemental dissolution rates (ν_M) were converted to an equivalent elemental current density (i_M) using Faraday's law, which is a comparable basis to electron current density. AESEC experiments were also performed in a 0.1 M NaCl pH 4 solution. Dissolution rates were monitored during fast and slow galvanostatic growth experiments until the recorded potential reached +0.2 V_{SCE} (Fig. 1a), and for the subsequent potentiostatic hold at +0.2 V_{SCE} (Fig. 1b).

The electrochemically formed passive films were subsequently characterized by X-ray photoelectron spectroscopy (XPS). XPS measurements were performed right after fast or slow galvanostatic growth or after the additional potentiostatic growth. Samples were inserted in a nitrogen backfilled bag immediately after extraction from solution and introduced to the XPS vacuum chamber within 1 h of finalizing the aqueous corrosion experiments. The samples were not subjected to any surface treatment, cleaning or sputtering cycles. The only contaminant observed on the surface from survey spectra was adventitious carbon albeit in small concentrations <5 at%. Supplementary Data Fig. S3 show a very small contribution to the O1s peak from adsorbed or residual water. Any other surface treatment and cleaning processes, or sputtering are destructive to the as-prepared film composition and structure, and, therefore, avoided. The passive film growth was replicated with the identical sample and processing conditions for the electrochemical tests including LSV. LSV alters the passive film and the sample can therefore not be used for XPS characterization. The portfolio of electrochemical tests is given in Fig. 1.

Measurements were taken with a Scienta Omicron Multiprobe MXPS with a monochromatic Al-Kα X-ray source ($h\nu$ = 1486.7 eV). The small information depth of XPS allows for the study of the chemical nature of nanometers scale passive films. AR-XPS (angle resolved XPS) is used to capture the depth distribution of species and elements within the passive layer. AR-XPS requires relatively smooth surfaces to allow for a meaningful interpretation of the data, and previous studies on Ni-22Cr in pH 4 NaCl solution, shows sub-nanometer root mean square (RMS) roughness values which is sufficient for the current work.[44]

Table I. Summary of experimental conditions and corresponding sample labels.

Experiment Label	Ni-22Cr [S]	Ni-22Cr [F]	Ni-22Cr[S +A]	Ni-22Cr[F +A]	Ni-22Cr-6Mo [S]	Ni-22Cr-6Mo [F]	Ni-22Cr-6Mo[S +A]	Ni-22Cr-6Mo[F +A]
Ni concentration (wt%)	78	78	78	78	72	72	72	72
Cr concentration (wt%)	22	22	22	22	22	22	22	22
Mo concentration (wt%)	0	0	0	0	6	6	6	6
Galvanostatic Hold Current (nA/cm^2)	0.1	100	0.1	100	0.1	100	0.1	100
Potentiostatic Hold Duration +0.2V SCE (ks)	N/A	N/A	10	10	N/A	N/A	10	10

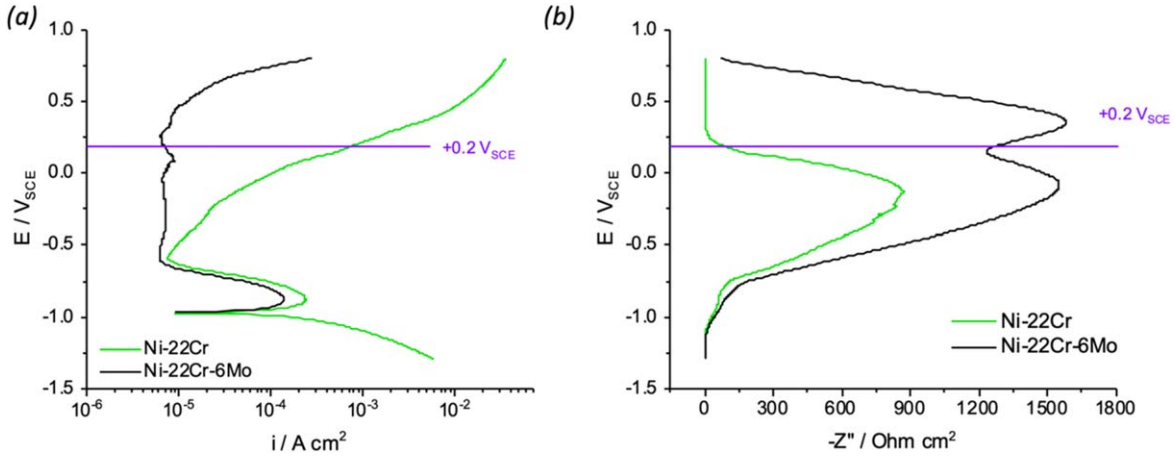

Figure 2. (a) E-log (i) polarization behavior of Ni-22Cr and Ni-22Cr-6Mo, and (b) imaginary impedance ($-Z''$) measurements during upward LSV scan of Ni-22Cr and Ni-22Cr-6Mo in deaerated 0.1 M NaCl pH 4 with the potential used in this study (+0.2 V_{SCE}) indicated.

The maximum information depth of a photoelectron is given by $d = 3\lambda \sin\theta$ where d is the information depth, λ is the inelastic mean free path of the photoelectron (IMFP), and θ is the take-off angle. For example, the inelastic mean free path (IMFP) for a Ni $2p_{3/2}$ electron from an Al-Kα source with a kinetic energy of 634.4 eV is 1.6 nm in $Ni(OH)_2$. Angle resolved measurements used take-off angles of 27.6° and 62.6°, which corresponds to information depth of approximately 2 and 4 nm, respectively[45] (geometry shown in Supplementary Data Fig. S1). For clarity in writing we will label the shallower take-off angle as "surface" and the larger take-off angle as "bulk." The passive layer thickness was calculated using the formalism developed by Carlson[46] and Strohmeier[47] for a uniform layer and is corrected for the take-off angle.

The O 1 s, Cr $2p_{3/2}$, Ni $2p_{3/2}$, and Mo 3d core levels were measured with 0.05 eV step size and 25 eV pass energy. XPS calibration was performed using the Au $4f_{7/2}$ peak referenced to 84.0 eV. A small shift attributed to charging of about ~0.5 eV to higher binding energies is observed for all alloy core levels and was corrected numerically using the position of the Ni $2p_{3/2}$ peak for Ni (0) referenced to 852.6 eV binding energy.[48] The Ni(0) peak is narrow, observed with high intensity for all samples and as such can be used as an internal reference to correct for charging. All XPS data were analyzed using the KolXPD software. Metal core levels were fitted with a Donjac Sunjic-Gaussian function to account for asymmetry.[49] All other peaks were fitted with Voigt lineshapes, and a Shirley background.[49,50]

For the fitting of the Cr $2p_{3/2}$ core level contributions from Cr(0), $Cr(OH)_3$, Cr_2O_3, and CrO_2 have been reported in the literature.[15,48,51] The peak fitting did not reveal any significant CrO_2, $NiCr_2O_4$ spinel or Cr(VI) contribution. Fitting of Cr(III) bound in $Cr(OH)_3$ and Cr_2O_3 included the requisite multiplet structure as taken from Biesinger et al.[48] and is herein shown as the multiplet envelope for clarity. $Cr(OH)_3$ can be fit using a single, broad Voigt peak. For the Ni $2p_{3/2}$ core level contributions from Ni (0) metal and its satellite, as well as $Ni(OH)_2$ were sufficient to achieve a good fit in all instances. $NiCr_2O_4$ spinel and NiO[48] were not detected, commensurate with the absence of a spinel signal in the Cr core level spectra. Other work supports our assessment and the passive layer is indeed defined by the oxide and hydroxide.[15] Fit examples for Ni and Cr with the multiplet structure resolved are presented in Supplementary Data Fig. S2. For Mo 3d, the Mo $3d_{5/2}$ and Mo $3d_{3/2}$ peaks for Mo(0), Mo(IV), and Mo(VI) oxidation states were included,[52] but the chemical state (oxide vs hydroxide) was not differentiated due to a relatively poor signal/noise ratio stemming from the small concentrations of Mo.

During all fitting procedures, the peaks belonging to different chemical species were constrained by their position (±0.5 eV), Gaussian half width (<0.5 eV with instrument resolution as the lower boundary), and relative intensity for peaks with a set ratio (±5%). For multiplet peaks, the relative peak position was fully constrained and consolidated in "fit envelopes" which then represent the unique chemical species. The same fit routine was used for all experimental conditions to ensure relative trends are preserved. Example of fit results for Ni, Cr, O, and Mo are presented later in Figs. 9–11, and the Supplementary Data. An example fit for Cr with multiplet contributions resolved into individual peaks and residuals plotted can be found in the Supplementary Data Figs. S2 and S3.

Results

The results of the upward LSV scan and imaginary impedance measurements are presented in Fig. 2 and illustrate the significant effect of alloying with Mo on passivity. The passive current density (i_{pass}) for Ni-22Cr-6Mo was two orders of magnitude lower than that of Ni-22Cr at +0.2 V_{SCE} (Fig. 2a). The potential +0.2 V_{SCE} was selected for the galvanostatic and potentiostatic experiments discussed here because of its relevance to the long-term open circuit potential of Ni-Cr-Mo alloys in seawater and other natural environments where passivation is sometimes punctuated by crevice corrosion.[9] Fig. 2a shows that +0.2 V_{SCE} is within the passive potential window of Ni-22Cr-6Mo but beyond the potential where the passive film often breaks down locally for Ni-22Cr. In Fig. 2b, the magnitude of $-Z''$ increased linearly with potential for $E > -1.0$ V_{SCE}, indicating film thickening linearly proportional to applied potential in the passive range, and reached a maximum value close to zero V_{SCE} followed by a decrease for $E > +0.1$ V_{SCE}. The addition of Mo resulted in lower passive current density, broadening of the passive region in the polarization curve (Fig. 2a), and greater values of $-Z''$ (Fig. 2b). These observations generally indicate the formation of a thicker, more stable passive film. The onset potential of transpassivity, indicated by the second peak in Z'', was also shifted to potentials above +0.5 V_{SCE} in the Ni-22Cr-6Mo samples due to Mo stabilizing the passive film in the presence of Cr(VI) transpassivity.[53,54]

Figure 3 shows the galvanostatic growth of the passive films and displays the potential increase as a function of time for the current densities of 100 $\mu A\ cm^{-2}$ and 0.1 $\mu A\ cm^{-2}$ for Ni-22Cr and Ni-22Cr-6Mo. A positive near-linear increase in potential with time, E (t), indicated passivation during the galvanostatic growth. In the case of the fast growth conditions (galvanostatic current $i_{app} = 100$ $\mu A\ cm^{-2}$) the potential reached +0.2 V_{SCE} for Ni-22Cr in less than 10 s after about 0.9 mC cm^{-2} of anodic charge density had passed. The same potential was reached for Ni-22Cr-6Mo in about 15 s with 1.5 mC cm^{-2} of anodic charge density passed. This behavior could indicate roughly linear thickening of the passive oxide film over time for the alloys undergoing fast passive film growth.

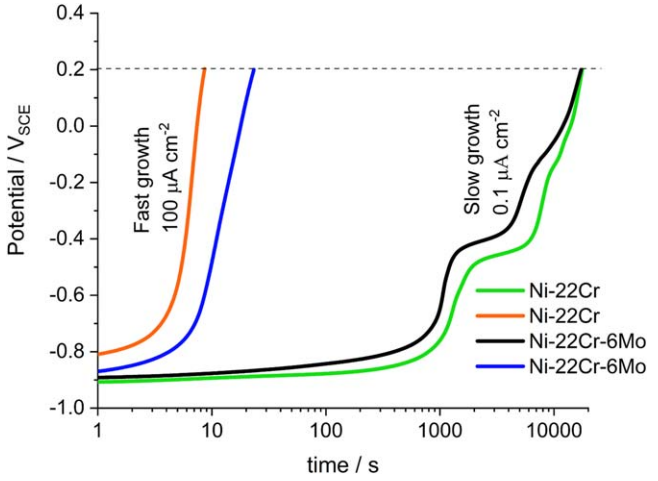

Figure 3. Galvanostatic growth of passive film on Ni-22Cr and Ni-22Cr-6Mo at fast galvanostatic (100 μA cm^{-2}) and slow galvanostatic (0.1 μA cm^{-2}) modes in deaerated 0.1 M NaCl pH 4. The potential was monitored until it reaches +0.2 V_{SCE} (horizontal dashed line).

For the slow growth conditions (galvanostatic current $i_{app} = 0.1$ μA cm^{-2}) the potential was reached for both alloys at approximately the same time—17.5 ks, after about 1.8 mC cm^{-2} of anodic charge density was passed. The potential increase might indicate passive film growth, and, vice versa, when there is no rise (plateau) in potential there could be passive film breakdown, a parallel oxidation reaction without protection film thickening or an entirely foreign oxidation reaction such as hydrogen oxidation seen at −0.9 V_{SCE}.[53] The slow growth curves both for Ni-22Cr and Ni-22Cr-6Mo contained brief potential-time plateaus, visible in Fig. 3, with different slopes E(t) from −0.8 V_{SCE} to −0.4 V_{SCE} and from −0.4 V_{SCE} to −0.1 V_{SCE}. These steps correlate to the passivity region beginning at −0.8 V_{SCE} and the maximum of −Z″ at −0.1 V_{SCE} (Fig. 2) and indicate the layering in the passive film with oxides of different molecular identity. In general, a high slope or fast potential rise indicates efficient passivation and facile growth.

As reported by Yu et al.[13] 1 nm of ideal compact rocksalt oxide with no porosity requires about 1.5–2 mC cm^{-2} of charge, and an extra 1 nm per mC cm^{-2} of passive films may be produced by porous outer hydroxides due to lower hydroxide density. Thus, passive film thicknesses from 1–2.5 nm for the 22Cr[F] and 22Cr6Mo[F] samples and 3–3.5 nm for the 22Cr[S] and 22Cr6Mo [S] might be expected from the galvanostatic growth electrochemical assessments. XPS thicknesses show the same trend.

Elemental dissolution rates were monitored by the AESEC technique in fast and slow galvanostatic growth experiments, as shown in Fig. 4. For the fast galvanostatic growth, an increase in Ni dissolution rate was monitored for both Ni-22Cr and Ni-22Cr-6Mo samples, as shown in Figs. 4a and 4b. A slight increase in Cr dissolution rate over time was observed as seen in Fig. 4a. For the slow galvanostatic growth (Figs. 4c and 4d), all elemental dissolution rates were below the detection limit except for Ni in Ni-22Cr (Fig. 4c) where a weak Ni dissolution peak was observed at t ∼ 1100 s. This suggests that fast growth is less efficient in terms of charge density devoted to insoluble oxide formation versus cation ejection.

The results of LSV and EIS are presented in Figs. 5 and 6. It is seen that 22Cr[F] and 22Cr6Mo[F] both display the analogous poorly protective E-log i corrosion behavior in the LSV curves (Fig. 5) and the lowest values of |Z| in the lowest frequency domain (1 mHz) after fast growth. The film on 22Cr[F] was grown galvanostatically, and further passivation at +0.2 V_{SCE} led to film breakdown and metal dissolution as seen by AESEC. As a result of breakdown and concurrent loss of passive film an increase in current densities was observed. The electrochemical conditions of slow growth [S] and slow growth with exposure aging [S+A] exhibit the highest corrosion resistivity according to LSV and EIS measurements for both alloys. For the slow growth samples, 22Cr[S] and 22Cr6Mo[S], both the passive and corrosion current were an order of magnitude lower than the passive and corrosion currents of fast grown samples [F] and [F+A], as seen in Figs. 5a and 5b. There was also a significant increase in impedance modulus in the low frequency domain (1 mHz $< f <$ 10 mHz) for 22Cr[S] and 22Cr6Mo[S] (Figs. 6a, 6b).

The potentiostatic hold "exposure aging" at +0.2 V_{SCE} was performed after the fast and slow growth for all samples (see Table I for details). Figure 7a shows the current density decay during 10 ks of potentiostatic hold at +0.2 V_{SCE}. An initial current density difference of two orders of magnitude was found between fast and slow grown samples for both alloys, Ni-22Cr and Ni-22Cr-6Mo, which is in agreement with the LSV results in Fig. 5. The analogous decay of the passive current density was observed for the slow growth Ni-22Cr and Ni-22Cr-6Mo samples (Fig. 7a) which could indicate a thickening of the passive film or annihilation of cationic film defects. A further increase of −Z″ and passive oxide film thickness l_{ox} calculated from Eq. 1 confirmed the passive film thickening expected (Fig. 7b) and.seen in the LSV (Fig. 5b).

The current decay and −Z″ for the fast growth sample displayed an entirely different progression with time. A rapid increase in current is seen for Ni-22Cr after 200–300 s of potentiostatic hold; this increase was evidence of the passive film breakdown indicated on Fig. 7b by the abrupt end to the orange line at 200 s. At the same time, the passive current density decreased gradually during the potentiostatic hold of the Ni-22Cr-6Mo fast growth sample until it was nearly equal to the passive current density of the Ni-22Cr-6Mo slow growth sample at 10 ks (Fig. 7a) towards the end of the potentiostatic hold. Figure 7b indicates approximately the same value of −Z″ and the corresponding estimated passive film thickness (∼3.2–3.4 nm) at the end of the measurement. Some metastable breakdown events evidenced by small spikes superimposed on the current trace were seen for the Ni-22Cr-6Mo fast growth sample and the Ni-22Cr slow growth sample after 2000 s of potentiostatic hold. For samples like Ni-22Cr, which are more prone to crevice corrosion, the higher current densities for t > 1000 s seen in Fig. 8c - AESEC experiment - and Fig. 7a - electrochemical experiment at UVA - are due to the related instability in passivation conditions.

LSV and EIS data confirmed that the additional potentiostatic growth "exposure aging" for the Ni-22Cr slow growth and Ni-22Cr-6Mo both slow and fast growth samples 22Cr[S+A], 22Cr6Mo[S +A], and 22Cr6Mo[F+A] samples, respectively, increased the passive film thickness and protectiveness towards corrosion: i_{pass} and i_{corr} decreased while Z_{mod} increased relative to the passive layers formed without aging (Figs. 5 and 6). The absence of the passive region on the LSV plot and drop of |Z| for 22Cr[F+A] sample are consequences of passive film breakdown and possibly crevice corrosion (Figs. 5a and 6a).

Elemental dissolution rates during potentiostatic hold at 0.2 V_{SCE} for 2000 ∼ 5000 s after fast and slow galvanostatic growth were also monitored by the AESEC technique for Ni-22Cr and Ni-22Cr-6Mo, shown in Fig. 8. For Ni-22Cr, the dissolution rates of Ni and Cr were above the detection limit and followed a similar trend in the case of fast galvanostatic growth (Fig. 8a). For slow oxidation, Cr was below the detection limit for t < 700 s as shown in Fig. 8c. For both fast and slow galvanostatic growth of Ni-22Cr, passive film breakdown is indicated by an increase in electric current density ($i_{e.}$) when t > 700 s as well as increase in elemental dissolution rates. The spikes of $i_{e.}$ signals observed for Ni-22Cr for t > 700 s in Figs. 8a and 8c could indicate metastable pitting events or crevice corrosion.

For Ni-22Cr-6Mo, the dissolution rate of Mo was below the detection limit after fast and slow galvanostatic growth during potentiostatic hold at +0.2 V_{SCE} (Figs. 8b and 8d). Similar to the results for the binary alloy, Ni and Cr dissolution rates in the ternary alloy increased for t > 800 s in the case of fast galvanostatic growth

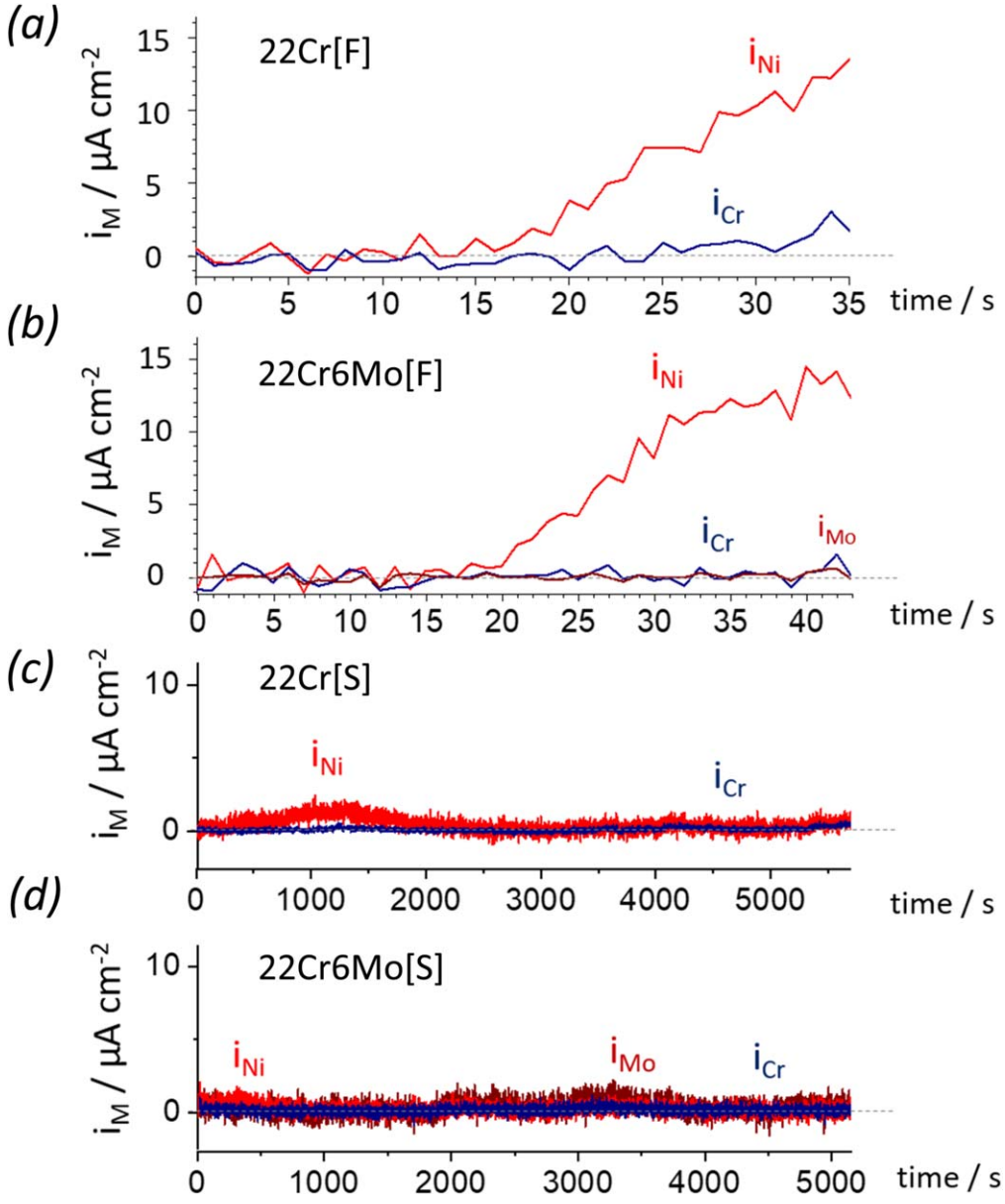

Figure 4. Elemental dissolution rates monitored by AESEC during fast and slow galvanostatic oxidation on Ni-22Cr (a), (c) and Ni-22Cr-6Mo (b), (d) samples in 0.1 M NaCl, pH 4 after 600 s of -1.3 V_{SCE} cathodic reduction.

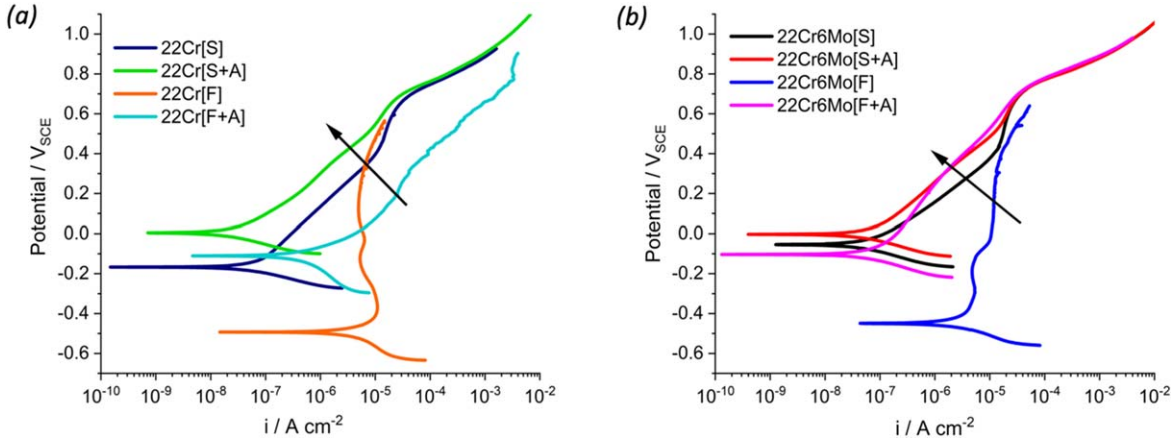

Figure 5. LSV (E-log (i) polarization) curves of (a) Ni-22Cr, and (b) Ni-22Cr-6Mo after the each galvanostatic oxidation in deaerated 0.1 M NaCl pH 4. Arrow indicates a decrease of passive current density.

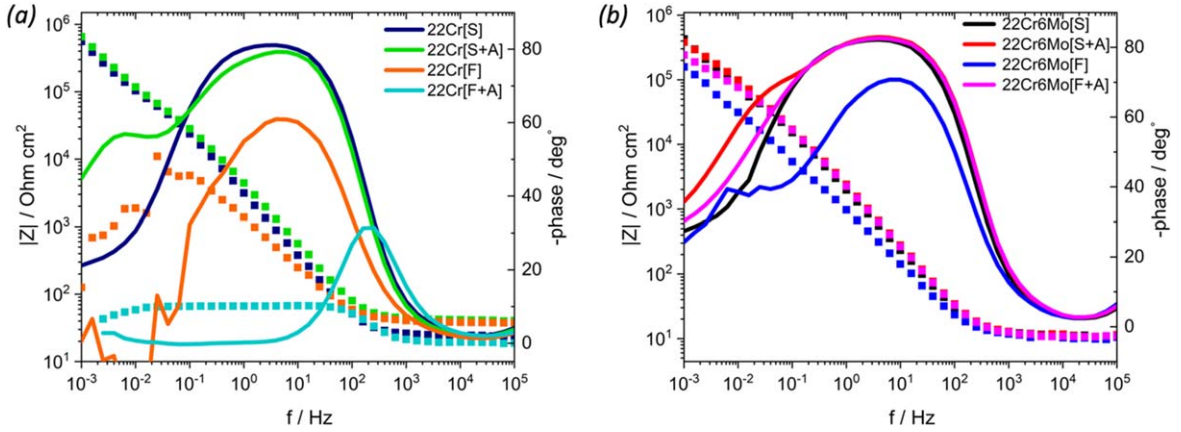

Figure 6. Bode and phase angle plots of Ni-22Cr (a) and Ni-22Cr-6Mo (b) after the each galvanostatic oxidation in deaerated 0.1 M NaCl pH 4.

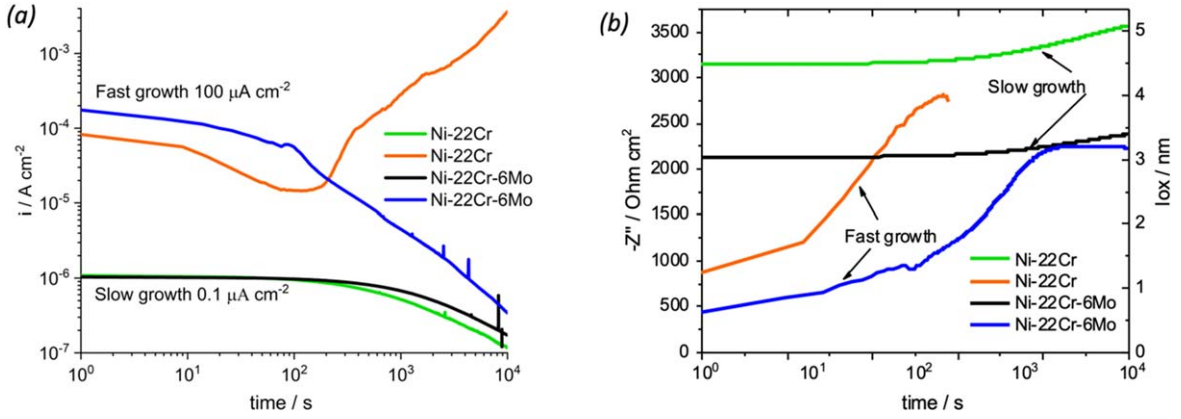

Figure 7. Potentiostatic hold at +0.2 V_{SCE} of Ni-22Cr and Ni-22Cr-6Mo for 10 ks in deaerated 0.1 M NaCl pH 4 after slow and fast galvanostatic growth: (a) current density vs time; and (b) imaginary impedance ($-Z''$) and oxide film thickness (l_{ox}).

(Fig. 8b). Moreover, less significant current spike peaks were monitored as compared with those of Ni-22Cr in Fig. 8a. This may indicate that the passive film formed by fast galvanostatic growth on Ni-22Cr-6Mo surface is more resistant to pitting corrosion compared to the Ni-22Cr passive film formed under identical conditions. For Ni-22Cr-6Mo after slow galvanostatic growth (Fig. 8d), all elemental dissolution was below the detection limit.

Compositional characterization of passive films.—For a better understanding of the nature of the passive films the electrochemical analysis is complemented by a study of film composition, element and chemical species distribution within the passive film using XPS. The Ni and Cr core level XPS spectra of Ni $2p_{3/2}$ and Cr $2p_{3/2}$ for Ni-22Cr and Ni-22Cr-6Mo are shown in Fig. 9 for all potentiostatic and galvanostatic passivation steps as defined in Table I. Figure 10 extracts the cation fractions for Cr(III) and Ni(II), and the fit procedure and error bars are tested by a comparison between O 1 s, Ni 2p and Cr 2p core level analysis and described in detail in the Supplementary Data Figs. S2 and S3. The angle dependent measurement delivers data on the distribution of hydroxide and oxide species through the thickness of the passive layer which is summarized in Fig. 11. The Mo 3d core level spectra are shown in Fig. 12.

The Ni $2p_{3/2}$ core levels in Fig. 9 consist of two components. The first is Ni(0) from the alloy signal with a main peak at 852.6 eV and satellite peak at 858.7 eV. The second is Ni(II) bound in $Ni(OH)_2$ with a multiplet beginning at 856.0 eV. The Cr $2p_{3/2}$ core level includes three components: Cr(0) from the alloy at 574.0 eV binding energy, $Cr(OH)_3$ and Cr_2O_3 in the passive layer which are represented by the envelope of the respective multiplets used to fit the chemically shifted core levels. No NiO or Cr(VI) is detected in any of the passive layers and their contribution, if any, is well below a 5% detection limit for mixed oxide/hydroxide films. The identity of the chemical species is consistent across all samples, but their relative contributions change with electrochemical conditions. Examples for the Cr $2p_{3/2}$ core level fit are shown in the SupplementaryData Fig. S2, where the individual components of the multiplet envelope are resolved. [48]

Inspection of the core levels summarized in Fig. 9 reveals a modulation of the spectral shape caused by a change in the ratio of alloy-to-oxide peak intensity, which reflects the passive layer thickness, and the modulation in the concentration of the different chemical species. The Ni(0) and Cr(0) components are clearly visible in all cases due to the small passive layer thickness. The $Cr(OH)_3$ peak dominates in most Cr 2p core levels and the Cr_2O_3 contributions are maximized after aging in Ni-22Cr[S+A]. The smallest Cr_2O_3 contribution is detected in Ni-22Cr-6Mo[S], followed by Ni-22Cr[F]. The thickness of the passive layer is between 0.8 nm for Ni-22Cr[S] and 2.3 nm for Ni-22Cr-6Mo[S]. The thickness calculated with the Strohmeier formulation[47] and from electrochemical analysis both include several assumptions and can therefore only be treated as rough approximations valid for the comparison of trends. The comparison of the oxide thickness calculated by the Z'' method with the thickness obtained from XPS has been reported[55] and they show a reasonable agreement with a difference in thicknesses within a factor of 1.3–2.0 times between the methods. This variation in thickness between the two methods is common, and has been reported by other corrosion studies for passive films on Cr-containing[24,42,44] and Al-containing alloys.[56,57]

Figure 10 summarizes the passive film composition as it relates to electrochemical processing for both alloys using bulk and surface

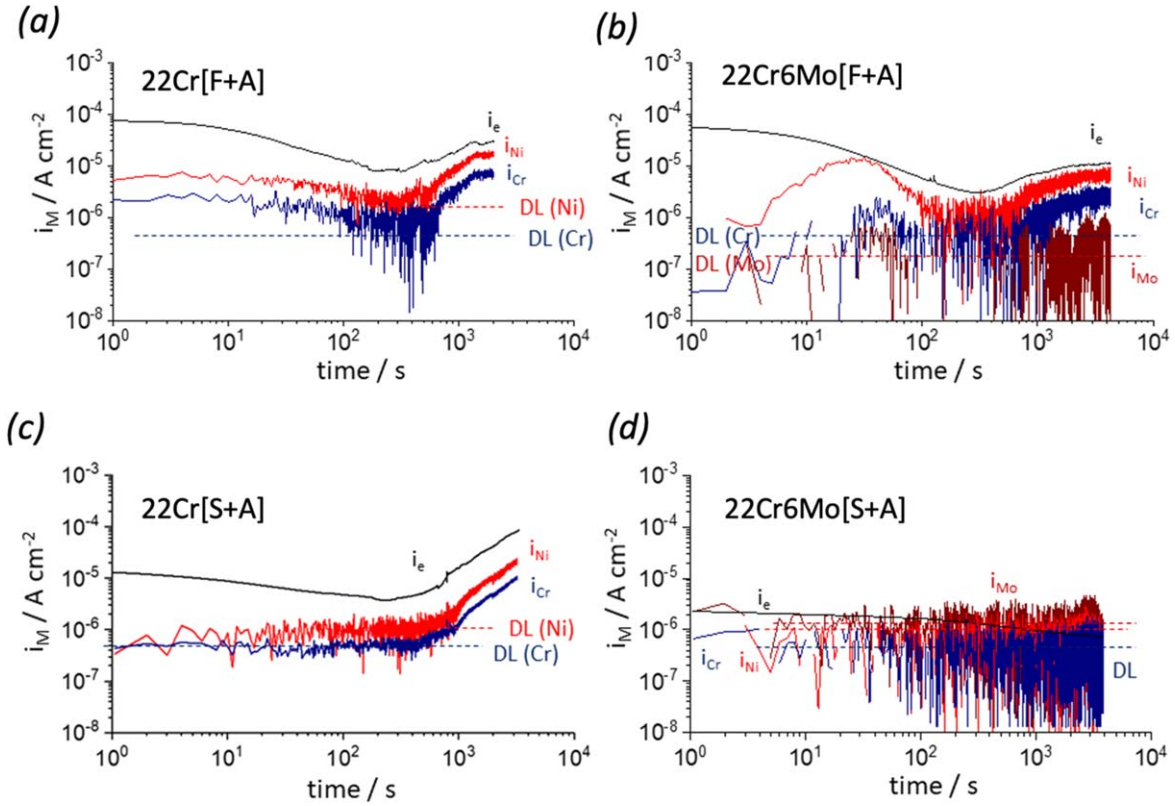

Figure 8. Elemental dissolution rates monitored by AESEC during the potentiostatic hold at +0.2 V_{SCE} after fast and slow galvanostatic oxidation on Ni-22Cr (fast (a) and slow (c)) and on Ni-22Cr-6Mo (fast (b) and slow (d)). The detection limits for Cr and Ni cations are indicted with a dotted line.

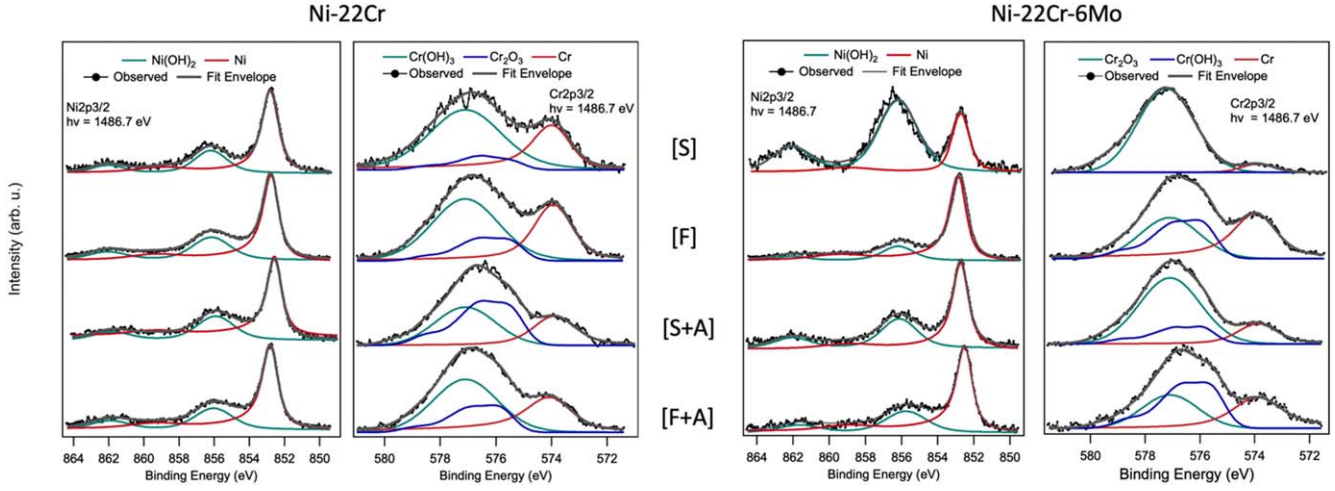

Figure 9. Ni and Cr core level spectra for Ni-22Cr (left) and Ni-22Cr-6Mo (right) for a take off angle of 27.6° (surface). Spectra are normalized to unit height and the background has been subtracted to facilitate comparison of spectral shapes.

sensitive measurements. The Fig. 10a is resolved by cation fraction with Cr(III) and Ni(II) balanced to one, whereas Cr(III) includes hydroxide and oxide contributions. Figure 10b includes the ternary alloy and Cr(III), Ni(II) and Mo(IV/VI) balanced to one. Cr was the dominant cation in the passive film for all electrochemical conditions of the Mo-containing alloy samples, and the exposure aged samples for Ni-22Cr[F+A]. Except for the samples Ni-22Cr[S] and [F], the cation fractions X_A are constant within the error of the measurement with Ni-22Cr-6Mo[S] at the upper boundary of the error interval, and Ni-22Cr-6Mo[S+A] at the lower boundary. In comparison, the enrichment of the passive layer in Cr for exposure aged [+A] Ni-22Cr, and in all ternary alloy samples is significant. In general, rapid growth favors Ni(II) while over time Cr(III) enriches.

The passive layer composition for the ternary alloy is near constant, and aging mostly influences hydroxide and Mo distributions throughout the film as discussed in Figs. 11 and 12. The variation in cation fraction between surface (27.6° take-off angle) and bulk (62.6° take-off angle) as assessed by AR-XPS (angle-resolved XPS) is for all samples within the range of the combined experimental error from the electrochemical processing, and the XPS fitting. The cation fraction, and hence distribution of Ni and Cr cations is constant throughout the passive layer within the precision of our XPS characterization. In the case of solute trapping which

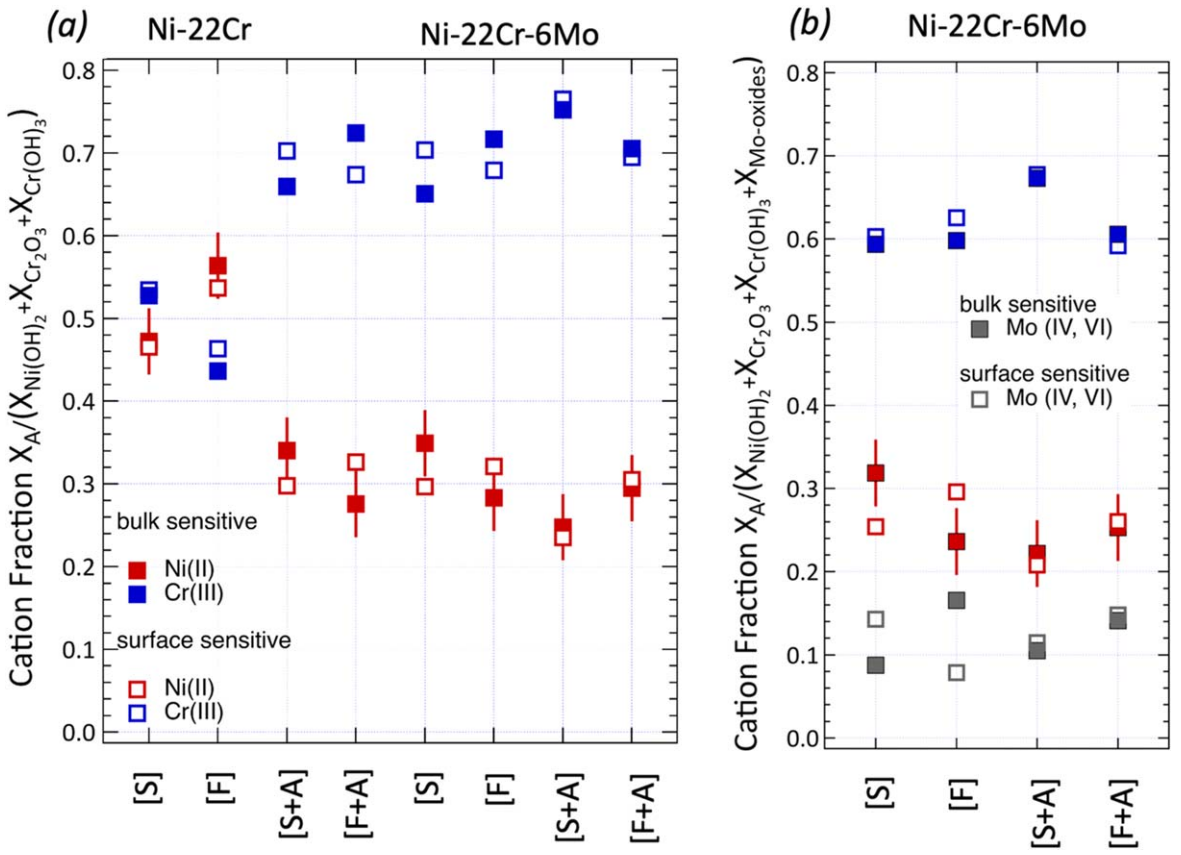

Figure 10. Fraction X_A of Ni (II) and Cr(III) in the passive film (a), and Ni(II), Cr(III) and Mo(IV,VI) (b). The margin of error is indicated for Ni(II) bulk sensitive datapoints and valid for all datasets. The Cr(III) fraction includes oxide and hydroxide contributions, Ni(II) is only present as hydroxide, and Mo(IV,VI) only as oxide.

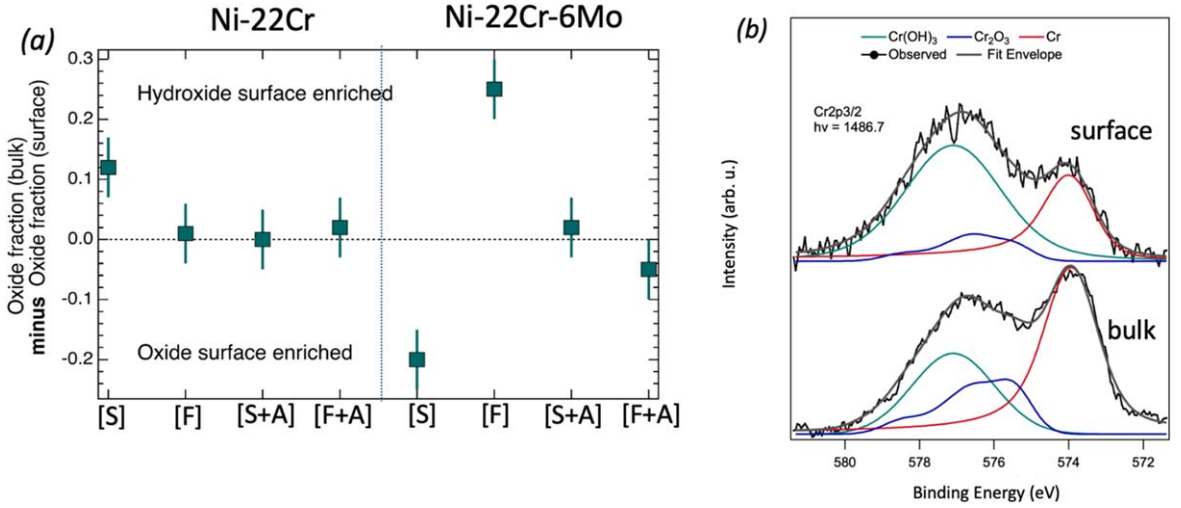

Figure 11. (a) Difference between oxide fraction (chromia) in the oxide bulk and oxide fraction at the surface. The difference is calculated from the numbers included in the Supplementary Data. A passive layer with a higher bulk contribution of oxide will be enriched in hydroxide at the surface. (b) an example of strong layering is illustrated in the Cr spectra for Ni-22Cr6Mo[F].

might be expected for fast growth samples, and has been described by Yu et al.,[35] the alloy composition would be reflected in the passive layer: Ni(II) contributions at 78% and Cr(III) at 22%. This is not observed, and even the lowest Cr(III) contribution reaches 45% (Fig. 10). This does not exclude some contribution of solute trapping, but even fast grown layer show an enrichment in Cr(III).

The fit process delivers the relative contributions of oxide (chromia) and hydroxide (Ni, and Cr hydroxides) for bulk and surface sensitive measurements. Figure 11 summarizes the difference between bulk and surface oxide fractions and illustrates the extent and type of stratification. A larger oxide fraction corresponds to a smaller hydroxide fraction in the passive layer. "Stratification" should not be understood as clearly separated distinct layers, but a variation in composition throughout the layer as we move from the alloy-passive layer interface (bulk) to the surface. The complete

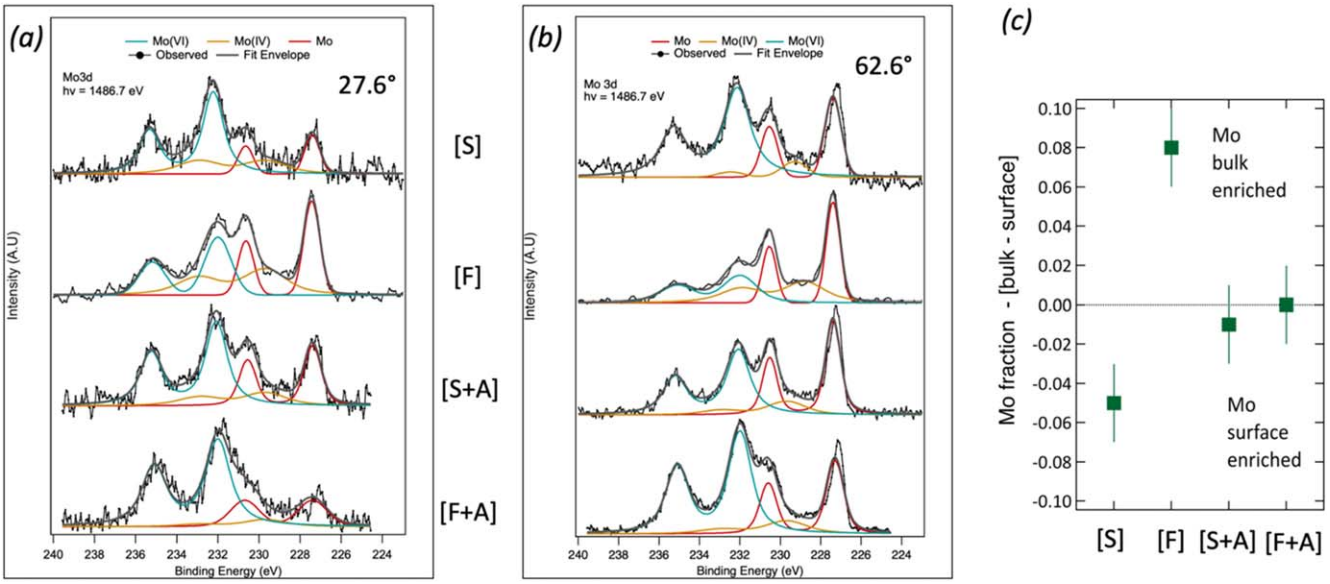

Figure 12. Mo core levels for the Ni-22Cr-6Mo sample with takeoff angle of 27.6° - more *surface* sensitive, and (b) 62.6° - more *bulk* sensitive. Spectra are normalized to unit height and a Shirley background is removed for visualization. (c) Comparison of Mo concentrations for bulk and surface sensitive angle settings.

dataset where surface and bulk contributions are resolved is presented in the Supplementary Data Figs. S3 and S4.

We initially assumed that an enrichment of the hydroxides at the surface will be common to all our samples,[10,17–19] but this is not the case. Most samples, Ni-22Cr [F, S+A, F+A] and Ni-22Cr-6Mo [S +A, F+A] show a uniform distribution of hydroxide and oxide throughout the passive layer. Only Ni-22Cr[S] and Ni-22Cr-6Mo[F] exhibit the expected enrichment of hydroxides at the surface. Finally, Ni-22Cr-6Mo[S] shows an inverted layering with more hydroxide closer to the interface with the alloy, with more oxide at the surface. This can also be seenin comparison between the original spectra for more bulk sensitive (Supplementary Data Fig. S5) and more surface sensitive (manuscript Fig. 9) for Ni-22Cr-6Mo[S] the $Ni(OH)_2$ contribution is larger for the more bulk sensitive spectra. The difference in oxide/hydroxide contributions exceeds the difference in cation fractions and is thus not solely due to an increase in $Ni(OH)_2$. The inverted layering scheme implies that the electrochemical oxidation process, which includes growth and dissolution events, is modified.

Figures 12a and 12b presents the Mo 3d spectra for all electrochemical processing conditions and for both take-off angles in Ni-22Cr-6Mo alloys. These spectra illustrate the distribution of Mo and its oxidation states throughout the passive film. The concentration of Mo summarized in Table II exceeds in all samples the concentration in the alloy and is lowest at 9 at% for [S] and the fast growth [F] of the passive layer promotes enrichment in Mo to 16 at%. The contributions from Mo (VI) are between 8 and 12 at%, with smaller contributions of Mo(IV) where the largest value of 8 at % is seen for [F+A]. The addition of the potentiostatic hold [A] produces a uniform distribution of Mo throughout the passive layer. This does not hold true for the [S] and [F] samples as shown in Fig. 12c: [S] is enriched in Mo at the surface, while for [F] a surface depletion is observed.

The fast-grown films [F] and [F+A] were not more corrosion resistant despite the higher concentration of Mo. Interestingly, the fast grown sample [F] had the highest fraction of Mo in the passive film, and at the same time the most Mo(IV), but exhibited the worst corrosion behavior of all Ni-22Cr-6Mo samples and a high i_{pass} (see Table III in Discussion section). The passive layer on the Ni-22Cr-6Mo[F] nonetheless outperformed Ni-22Cr[F] which implies that the oxidation state of Mo can be important and predicting corrosion performance based solely on Mo concentration is not sufficient. In addition, film morphology and presumably accumulation of defects during fast growth can override the benefits of high Mo content.

We observe that the fraction of Mo in the passive film is correlated to the fraction of Cr_2O_3 in the passive film as illustrated in Fig. 13. Datapoints from all measurements discussed above are included in this figure: more Mo in the passive film is connected with larger percentages of Cr_2O_3 and consequently smaller contributions from $Cr(OH)_3$. This correlation can also be seen in comparison between Figs. 11b and 12c: Ni-22Cr-6Mo[S] is surface enriched in chromia and Mo, the opposite holds true for Ni-22Cr-6Mo[F]. Mo inclusion in the passive film appears to promote the overall Cr_2O_3 formation and discourage $Cr(OH)_3$ formation.

Discussion

The electrochemical tests showed that the slow galvanostatic growth conditions (0.1 μA cm^{-2}) [S] provided more protective oxide film than fast galvanostatic growth conditions (100 μA cm^{-2}) [F] Fig. 3. [S] grown passive films and those which were exposure aged tend to be slightly thicker than [F] grown films on the same alloy. The outcome of the electrochemical experiments is parameterized in the values of i_{pass} and |Z| and summarized in Table III.

Table II. Mo concentrations in the passive layer for all ternary alloy samples.

Experiment label	22Cr6Mo[S]	22Cr6Mo[F]	22Cr6Mo[S+A]	22Cr6Mo[F+A]
Mo/(Ni+Cr+Mo) bulk	9 at%	16 at%	10 at%	14 at%
Surface	14 at%	8 at%	11 at%	14 at%
Mo IV (bulk)	1 at%	8 at%	2 at%	2.5 at%
Mo VI (bulk)	8 at%	8 at%	8 at%	11.5 at%

Table III. Summary of electrochemical parameters relevant for quantification of passive layer performance including i_{pass} and |Z|. #1 to #3:: very good performances, #4 and #5: good performance, and #6 to #8: poor performance. Notes: (a) breakdown of passive film during |Z| measurement. (b) Film characteristics change with time—an unfavourable i_{pass} at the start of the measurement improved over time. The i_{pass} cited here was obtained at +0.2 V_{SCE}, (c) breakdown of passive layer film during |Z| measurement.

	i_{pass} A cm^{-2}	|Z|, ohm cm^2 (at 1 mHz)
1.Ni-22Cr[S+A]	$3.60{\cdot}10^{-7}$	$6.59{\cdot}10^{5}$
2. Ni-22Cr-6Mo[S+A]	$6.06{\cdot}10^{-7}$	$3.83{\cdot}10^{5}$
3. Ni-22Cr-6Mo[F+A]	$6.30{\cdot}10^{-7}$	$2.42{\cdot}10^{5}$
4. Ni-22Cr-6Mo[S]	$1.65{\cdot}10^{-6}$	$1.58{\cdot}10^{5}$
5. Ni-22Cr[S]	$1.92{\cdot}10^{-6}$	$5.59{\cdot}10^{5}$
6. Ni-22Cr[F] (a)	$5.21{\cdot}10^{-6}$	(126.30)
7. Ni-22Cr-6Mo[F] (b)	$1.18{\cdot}10^{-5}$	$1.58{\cdot}10^{5}$
8. Ni-22Cr[F+A] (c)	$2.39{\cdot}10^{-5}$	43.12

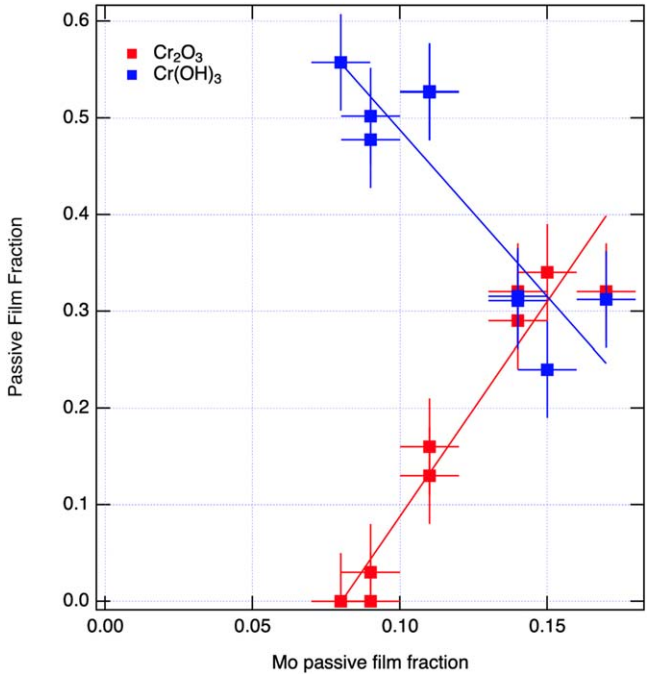

Figure 13. Relation between the fraction of Mo in the passive film and the fraction of chromia Cr(III). The figure includes all datasets presented in this manuscript with surface and bulk information. Linear trendlines are added to assist in visualization. The contributions from $Ni(OH)_2$ + $Cr(OH)_3$ + chromia are summed to 1.

These data are derived from the material presented in Figs. 5, 6 and 8. It shows in one place the beneficial passive behavior in galvanostatically slow-grown samples denoted by [S] for both alloys, Ni-22Cr and Ni-22Cr-6Mo. The subsequent potentiostatic aging of these samples led to further improvement in passivity (lower i_{pass} (Fig. 5)) and corrosion protection (lower i_{corr} and higher |Z| (Figs. 5 and 6)). The *fast* growth conditions did not provide a passive film with good corrosion-resistant properties for either Ni-22Cr or Ni-22Cr-6Mo. Furthermore, elemental dissolution was found by AESEC in both fast growth samples denoted by [F] (Figs. 4 and 8) which indicates inefficient passivation and also indicates the film breakdown by metastable pitting events or crevice corrosion. Indeed, the [F] samples show poor performance and breakdown at different points of electrochemical growth and testing. Only Ni-22Cr-6Mo[F+A] exhibits reasonable passivity.

The subsequent potentiostatic exposure aging led to improvement in the passivity of the film on the surface of Ni-22Cr-6Mo (lower i_{pass} (Fig. 5)) and corrosion protection (lower i_{corr} and higher |Z| (Figs. 5 and 6)). AESEC data (Figs. 4 and 8) also showed that Mo addition led to lower dissolution rates of all elements. The cation fraction of Cr and Ni in the passive film of the Ni-22Cr-6Mo remained relatively constant, while in the Ni-22Cr longer sample exposures to solution significantly altered the balance of Ni and Cr in the passive film. These results reveal that the conditions of film growth influence passivity, and corrosion protection for all alloys, and confirms the significant impact of the minor alloying element Mo.

We can now study the correlation between passive film characteristics measured with XPS and corrosion performance. The passive layer characteristics derived from analysis of the XPS data include Cr(III) concentration balanced by Ni(II) in $Ni(OH)_2$, Cr_2O_3 versus $Cr(OH)_3$ contributions, Mo cation contributions, element and hydroxide distribution throughout the passive layer, and film thickness. This information is included in Figs. 9–13. No parameter emerges as the sole determinant for a good passive layer, but several are clearly highly relevant, while others play a minor role.

Figure 14 summarizes the progression from [F] to [S] to [S+A] for Ni-22Cr and corresponds to the progression in ageing. The progression from fast to slow kinetics is accompanied by an increase in Cr(III) bonded in Cr_2O_3. At the same time the Cr-hydroxide percentage decreases, with a diminishing $Ni(OH)_2$ contribution. For Ni-22Cr[F+A] the Cr_2O_3 concentration lies between the values for [S] and [S+A] albeit with a disproportionately higher $Cr(OH)_3$ percentage. All values are summarized in the Supplementary Material S4—Table S1.

The presence of Cr(III) is in the literature generally associated with improved passivity and a Cr(III) cation fraction of 0.7 is reached for the majority of the passive films except for Ni-22Cr[S] and [F] (Fig. 10). Ni-22Cr[S] shows good passivity despite a lower Cr(III) fraction, while Ni-22Cr[F] and [F+A] perform poorly even though their Cr(III) fraction is high, and the same is true for Ni-22Cr-6Mo[F]. A higher Cr(III) fraction alone is not always sufficient to improve passivity in fast grown passive films. However, all ternary alloys possess a high Cr(III) cation fraction which is evident from Fig. 13 which establishes a clear correlation between Mo cation fraction in the passive film and the presence of Cr(III) and specifically the contribution of Cr_2O_3. Films marked with excellent performance in Table III tend to have a Cr_2O_3 fraction exceeding 0.3 with the balance to 1 attained by the addition of the hydroxides, $Cr(OH)_3$ and $Ni(OH)_2$. The exception is Ni-22Cr-6Mo[S+A] which is low in Cr_2O_3 but has one of the highest $Cr(OH)_3$ contributions, and is consequently low in $Ni(OH)_2$. In conclusion: a high contribution of Cr(III) cations often promotes passivity, and these cations can be present as oxide or hydroxide.

Aqueous exposure aging increases the Cr_2O_3 fraction for all alloys. Note that this is balanced by a low concentration of $Ni(OH)_2$ to conserve the overall Cr(III) cation fraction in oxide and hydroxide bonding environments of 0.7 (0.3 for Ni(II)). The presence of Cr(III) cations in the passive film can be promoted (a) through a preference in the nucleation of Cr(III) compounds due to the presence of Mo in agreement with Fig. 13, (b) the modification of relative dissolution rates for the various oxide and hydroxide components in Mo-containing passive layers, and (c) by exposure aging which drives the solid state reactions in the passive film towards the thermodynamically favored Cr(III) compounds.

Other passive film parameters established by the XPS analysis such as layering of hydroxides (Fig. 11) and small fluctuations in cation fractions between bulk and surface measurements (Fig. 10) are not indicated herein as primary factors that govern passivity. Ni-22Cr[S] with a good performance has a hydroxide enriched surface, while equally well performing Ni-22Cr-6Mo[S] shows inverted layering. The most extreme surface hydroxide enrichment is seen in Ni-22Cr-6Mo[F] which is a poorly performing layer. No trend with respect to performance can be established, but the observed

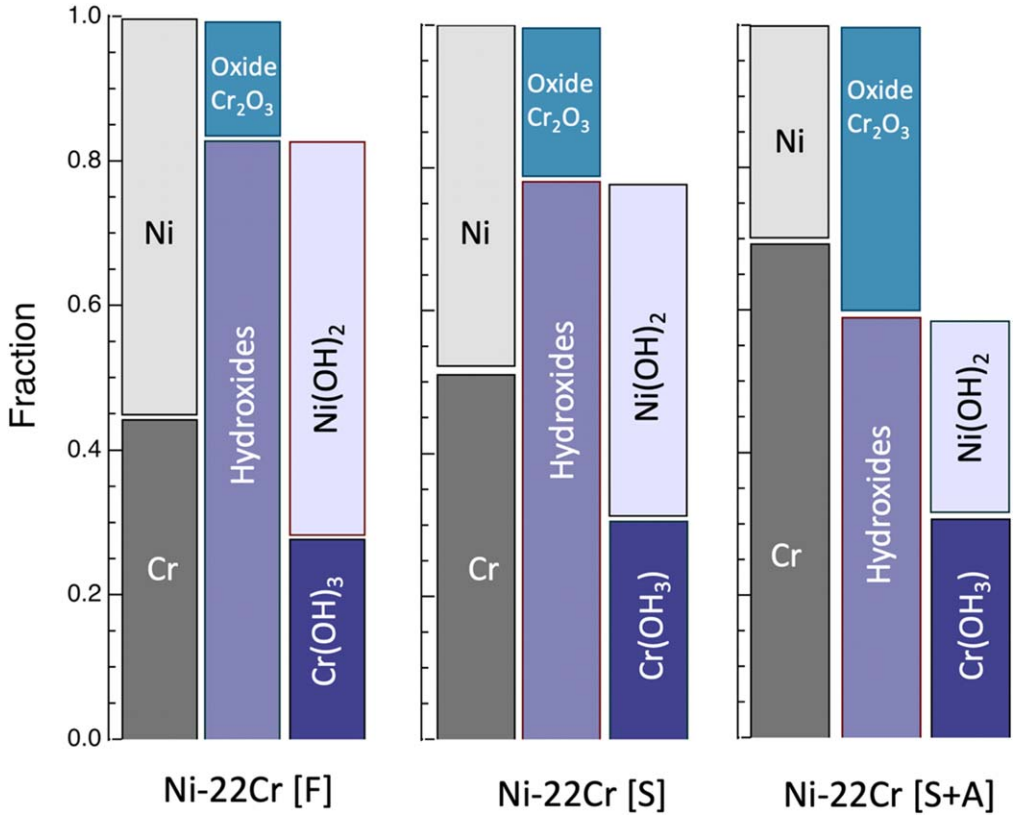

Figure 14. Change in passive layer composition and chemistry for Ni-22Cr with progressively slower growth kinetics from Ni-22Cr [F] to [S] and exposure ageing [S+A].

layering might offer insight on the mechanisms of passive layer growth.

Lastly, we address the role of Mo in impacting the performance of the passive layer. Mo is found in the oxide in several oxidation states. It is stratified and exists enriched in the bulk of the oxide and at the surface relative to the bulk alloy composition except for Mo (IV). Most passive layers grown on the ternary alloys perform well except for Ni-22Cr-6Mo[F]. This suggests that the solute vacancy interaction model or generally solute point defect interactions may be operative.[12] Indeed, all evidence points towards Mo cations in the oxide playing a role in point defect regulation or mediation. For instance, lower i_{pass}, increased |Z| at 1 mHz, changes in Mott-Schottky defect densities were all seen.[58] However, the Mo cation fraction is highest in the poorest performing layer and we assume that oxidized Mo is trapped within the rapidly growing passive layer and hence cannot perform its function for repair and stabilization of passivity.[5,8,24] In addition, Mo(IV) is highly prevalent in these samples. It is possible that the large concentration of defects in a rapidly grown passive layer, such as Ni-22Cr-6Mo[F], simply overwhelms the capacity of Mo to sequester enough defects to retain passivity.[59] Exposure aging, on the other hand, greatly improves performance and establishes a Mo(VI) to Mo(IV) ratio of about 4, which is also seen in the [S] sample. At the same time Mo becomes more evenly distributed within the passive layer which might enhance its function .

The rapid growth used in all [F] samples is detrimental to performance and cannot be mitigated in its entirety by favorable composition markers. We hypothesize that rapid growth introduced a significant number of defects, most likely point defects, within the passive layer which promote breakdown. The relation between defect concentration and growth rate has been established in thin film deposition and is captured in the structure zone model introduced by Thornton.[59] The rapid growth of the passive layer will tend to incorporate a large number of defects. For [S] samples the initial defect concentration should be significantly lower, but their performance can nonetheless benefit from exposure aging. The largest impact of [A] is indeed seen in Ni-22Cr[S] and Ni-22Cr-6Mo [S] which moves from good to very good passivity markers as summarized in Table III.

The AESEC data supports the XPS findings: Ni(II) is lost to the electrolyte in the case of [F] and [S] leading to increase in Cr(III) in the passive film. Significant loss of Ni(II) is due to direct ejection into the electrolyte and this occurs after 20 s during fast galvanostatic growth. However, the starting point is nearly 50% Ni(II) which means there is still relatively low passive film Cr(III) content. This is so even though nearly 100% Cr(III) at any instant joins the passive film during fast or slow exposure as seen in AESEC. The [S] condition is consistent with solute trapping, defect generation and, at least temporarily, non-equilibrium levels of defects. It is clearly associated with poor performance in both DC and AC electrochemistry which interrogate the passive state. Slow Ni(II) loss over the long term is chemically operative at pH 4 and thermodynamically supported. Defect generation is likely. In contrast Cr(III) is enriched during [S] and [+A] as well as with Mo alloying. Both AESEC and XPS support this. Defects have a chance to anneal out during [S+A] due to the longer time available for diffusive processes. Ni(II) is lost more slowly [S+A] and defects may annihilate at sinks. This is seen in AESEC by minor Ni(II) loss which happens over extended time periods. Nearly 100% Cr(III) joins the passive film leading to improved protection. In summary a number of processes and phenomena regulates the role of passivation on corrosion protectiveness.

Conclusions

The passive layer formation kinetics in acidic NaCl solution were modulated by using slow and fast galvanostatic growths in combination with potentiostatic aqueous exposure ageing. Ni-22Cr, and the complementary ternary alloy, Ni-22Cr-6Mo were studied using

electrochemical characterization, in situ atomic emission spectro-electrochemistry, and chemical analysis using X-ray photoelectron spectroscopy to deliver insight in the role of kinetics and exposure ageing on passive layer characteristics that affect protectiveness provided by passivation. Cr-rich hydroxides and oxides, and Ni(II) as Ni-hydroxide are bound in the passive film layer, and doping with aliovalent ions Mo(IV), Mo(VI) provides higher protectiveness towards corrosion relative to Ni-Cr binary alloys.

The correlation between passivity markers |Z| and i_{pass} and passive layer chemistry is complex and slower growth kinetics, exposure ageing, and Mo-doping promote Cr-integration in the passive layer, either as Cr-oxide or as hydroxide. Protectiveness can not be defined by just Cr and Mo alloy composition. For instance, fast growth kinetics are always detrimental to passive layer performance. Exposure aging promotes favorable composition markers such as an increase in Cr_2O_3 fraction and reduction in Ni-hydroxides, increase in film thickness, and higher Mo fraction (ternary alloys). At the same time, layering with respect to oxide and hydroxide distribution disappears or is at least weakened with exposure ageing. We propose that the diminished heterogeneity of the passive layer provides additional performance advantages. Mo is beneficial for all passive films in several ways. It encourages the formation of Cr_2O_3 over $Cr(OH)_3$, but cannot mitigate the shortcomings of fast growth conditions. The role of Mo is twofold—it promotes the formation of Cr_2O_3 over Cr- and Ni-hydroxides and it is argued in the literature that it sequesters defects within the passive layer thus acting as a "defect regulating agent" as well as the historically assumed "repair agent" function limiting damage from adverse passivity compressing events. The addition of Mo as a minor alloying element improves passivity unless the ability of Mo to sequester defects is overwhelmed, possibly by a large defect concentration created during the fast galvanostatic growth step. Hence a large concentration of Mo is an indicator of good performance but only in the context of the passive layer growth conditions.

It is evident that a single compositional marker such as Cr_2O_3 or Cr(III) fraction, Mo concentration, or Ni/Cr cation ratio is insufficient to ascertain performance of a passive layer. Our work shows that correlation between passive layer performance and passive layer chemistry is more fully captured in a "decision tree" type assessment, where multiple electrochemical and compositional parameters are integrated.

Acknowledgments

This work was supported by the Office of Naval Research under MURI "Understanding Atomic Scale Structure in Four Dimensions to Design and Control Corrosion Resistant Alloys" through Northwestern University #SP0028970-PROJ0007990-MURI ONR N00014–16–1–2280 under the directorship of Dr. Dave Shifler. K. O. and P. R. gratefully acknowledge the support by NSF DMR Metals and Metallic Nanostructures award #2004326. Author K. Ogle was supported by the Agence Nationale de Recherche, ANR-20-CE08-0031 (TAPAS 2020).

Statement of Work

E.R. performed the electrochemical experiments, including growth of passive films and electrochemical characterization. K.O. lead the XPS experiments with contributions from A.C., and K.O. was responsible for XPS fitting and data analysis. J.H. and K. Ogle contributed the AESEC study. K.O. and E.R. wrote the majority of the manuscript. J.S. and P.R. contributed to the writing of the manuscript, conceived and lead the study. All authors read and critiqued the manuscript.

ORCID

Keithen Orson https://orcid.org/0000-0001-8547-5387
Elena Romanovskaia https://orcid.org/0000-0001-8815-356X
Junsoo Han https://orcid.org/0000-0001-9295-2954
Petra Reinke https://orcid.org/0000-0002-4544-5906

References

1. R. Darolia, *Int. Mater. Rev.*, **64**, 355 (2019).
2. C. D. Taylor, P. Lu, J. Saal, G. S. Frankel, and J. R. Scully, *Npj Mater Degrad*, **2**, 6 (2018).
3. X. Li et al., *Corros. Sci.*, **176**, 109015 (2020).
4. R. Auguste et al., *Npj Mater Degrad*, **6**, 61 (2022).
5. K. Lutton Cwalina, C. R. Demarest, A. Y. Gerard, and J. R. Scully, *Curr. Opin. Solid State Mater. Sci.*, **23**, 129 (2019).
6. K. Lutton, K. Gusieva, N. Ott, N. Birbilis, and J. R. Scully, *Electrochem. Commun.*, **80**, 44 (2017).
7. E. Romanovskaia, K. Lutton, M. Amalraj, L. Marks, and J. R. Scully, *ECS Meeting Abstracts*, **MA2022-02**, 711711 (2022).
8. A. C. Lloyd, J. J. Noël, S. McIntyre, and D. W. Shoesmith, *Electrochim. Acta*, **49**, 3015 (2004).
9. R. S. Lillard, M. P. Jurinski, and J. R. Scully, *Corrosion*, **50**, 251 (1994).
10. Z. Wang et al., *J. Electrochem. Soc.*, **168**, 041503 (2021).
11. Z. Wang et al., *Appl. Surf. Sci.*, **576**, 151836 (2022).
12. M. Urquidi and D. D. Macdonald, *J. Electrochem. Soc.*, **132**, 555 (1985).
13. X. X. Yu, J. Han, J. R. Scully, and L. D. Marks, *Acta Mater.*, **213**, 116898 (2021).
14. Y. M. J. Y. T. Sun, X. Tan, L. L. Lei, and J. Li, *Tungsten*, **3**, 329 (2021).
15. A. Larsson et al., *J. Alloys Compd.*, **895**, 162657 (2021).
16. J. Eidhagen et al., *J. Electrochem. Soc.*, **170**, 021506 (2023).
17. P. M. A. Machet, A. Galtayries, S. Zanna, L. Klien, V. Maurice, P. Jovilet, M. Foucalt, P. Combrade, and P. Scott, *Electrochimica Acta*, **49**, 3957 (2004).
18. M. Långberg et al., *Npj Mater Degrad*, **3**, 22 (2019).
19. M. Långberg et al., *Corros. Sci.*, **174**, 108841 (2020).
20. P. Jakupi, D. Zagidulin, J. J. Noël, and D. W. Shoesmith, *Electrochim. Acta*, **56**, 6251 (2011).
21. H. H. Strehblow, *Electrochim. Acta*, **212**, 630 (2016).
22. A. C. Lloydis, J. J. Noël, D. W. Shoesmith, and N. S. McIntyre, *JOM*, **57**, 31 (2005).
23. X. Zhang, D. Zagidulin, and D. W. Shoesmith, *Electrochim. Acta*, **89**, 814 (2013).
24. K. L. Cwalina et al., *J. Electrochem. Soc.*, **166**, C3241 (2019).
25. J. R. Scully, E. Romanovskaia, K. Lutton, A. Y. Gerard, and S. B. Inman, *ECS Meeting Abstracts*, **MA2022-02**, 733733 (2022).
26. A. Y. Gerard et al., *Acta Mater.*, **245**, 118607 (2023).
27. K. Lutton et al., *J. Electrochem. Soc.*, **170**, 021507 (2023).
28. P. M. A. Seyeux, Z. Wang, S. Zanna, C. Carriere, and D. Mercier, *Electrochim. Acta*, **426**, 140797 (2022).
29. P. Marcus, *Corrosion Mechanisms in Theory and Practice* (Boca Raton, FL)(CRC Press) (2011).
30. C. R. Clayton and Y. C. Lu, *J. Electrochem. Soc.*, **133**, 2465 (1986).
31. J. D. Henderson et al., *J. Electrochem. Soc.*, **168**, 021509 (2021).
32. M. Karri, A. Verma, J. B. Singh, S. K. Bonagani, and U. K. Goutam, *Corrosion*, **78**, 228 (2022).
33. A. Verma, J. B. Singh, S. D. Kaushik, and V. Siruguri, *J. Alloys Compd.*, **813**, 152195 (2020).
34. D. Zagidulin, X. Zhang, J. Zhou, J. J. Noël, and D. W. Shoesmith, *Surf. Interface Anal.*, **45**, 1014 (2013).
35. X. X. Yu et al., *Phys. Rev. Lett.*, **121**, 145701 (2018).
36. N. Sato, *J. Electrochem. Soc.*, **129**, 255 (1982).
37. K. Gusieva et al., *J. Phys. Chem. C*, **122**, 19499 (2018).
38. D. D. Macdonald, A. Sun, N. Priyantha, and P. Jayaweera, *J. Electroanal. Chem.*, **572**, 421 (2004).
39. K. V. Rao and A. Smakula, *J. Appl. Phys.*, **36**, 2031 (1965).
40. A. Motori, F. Sandrolini, and G. Davolio, *J. Power Sources*, **48**, 361 (1994).
41. K. F. Quiambao et al., *Acta Mater.*, **164**, 362 (2019).
42. A. Y. Gerard et al., *Acta Mater.*, **198**, 121 (2020).
43. K. Ogle and S. Weber, *J. Electrochem. Soc.*, **147**, 1770 (2000).
44. P. Lutton, K. Blades, W. Scully, and J. Reinke, *J. Phys. Chem. C*, **124**, 9289 (2020).
45. C. Powell and A. Jablonski, *NIST Elastic Inelastic-Mean-Free-Path Database* (Gaithersburg, MD)(National Institute of Standards and Technology) (2010), Version 1.2, SRD 71..
46. T. A. Carlson, *Surf. Interface Anal.*, **4**, 125 (1982).
47. B. R. Strohmeier, *Surf. Interface Anal.*, **15**, 51 (1990).
48. M. C. Biesinger et al., *Appl. Surf. Sci.*, **257**, 2717 (2011).
49. S. Doniach and M. Sunjic, *J. Phys. C*, **3**, 285 (1970).
50. J. E. Castle and A. M. Salvi, *Journal of Vacuum Science & Technology A: Vacuum, Surfaces, and Films*, **19**, 1170 (2001).
51. B. P. Payne, M. C. Biesinger, and N. S. McIntyre, *J Electron Spectros Relat Phenomena*, **184**, 29 (2011).
52. J. Baltrusaitis et al., *Appl. Surf. Sci.*, **326**, 151 (2015).
53. J. D. Henderson, X. Li, D. W. Shoesmith, J. J. Noël, and K. Ogle, *Corros. Sci.*, **147**, 32 (2019).
54. B. Kobe et al., *Surface and Interface Analysis*, **49**, 1345 (2017).
55. A. M. Panindre, Y. Khalifa, C. D. Taylor, and G. S. Frankel, *J. Electrochem. Soc.*, **168**, 031513 (2021).
56. J. Evertsson et al., *Appl. Surf. Sci.*, **349**, 826 (2015).
57. F. J. Martin, G. T. Cheek, W. E. O'Grady, and P. M. Natishan, *Corros. Sci.*, **47**, 3187 (2005).

58. K. Lutton Cwalina, "Electrochemical passivation of Ni-Cr and Ni-Cr-Mo alloys: the fate of alloying elements and implications of oxide dopants and defects towards passivation and breakdown. University of Virginia, materials science - school of engineering and applied science." *PhD-Thesis* (2019).

59. J. A. Thornton, *Proc. SPIE, Modeling of Optical Thin Films*, *31st Annual Technical Symposium on Optical and Optoelectronic Applied Sciences and Engineering*, San Diego, CA, ed. M. R. Jacobson **Vol. 0821**, p. 95 (1987).